

RESEARCH ARTICLE

10.1029/2018JB016932

This article is a companion to Miyazaki and Korenaga (2019), <https://doi.org/10.1029/2018JB016928>.

Key Points:

- A new method to construct a thermodynamic model from melting experiments is presented
- Our method can constrain all thermodynamic model parameters simultaneously
- The thermal expansivity of SiO₂ and the excess volume of mixing between MgO and SiO₂ are shown to be the key parameters

Correspondence to:

Y. Miyazaki,
yoshinori.miyazaki@yale.edu

Citation:

Miyazaki, Y., & Korenaga, J. (2019). On the timescale of magma ocean solidification and its chemical consequences: 1. Thermodynamic database for liquid at high pressures. *Journal of Geophysical Research: Solid Earth*, 124, 3382–3398. <https://doi.org/10.1029/2018JB016932>

Received 24 OCT 2018

Accepted 27 JAN 2019

Accepted article online 18 MAR 2019

Published online 5 APR 2019

On the Timescale of Magma Ocean Solidification and Its Chemical Consequences: 1. Thermodynamic Database for Liquid at High Pressures

Yoshinori Miyazaki¹  and Jun Korenaga¹ 

¹Department of Geology and Geophysics, Yale University, New Haven, CT, USA

Abstract We present a new method to construct an internally consistent thermodynamic model using a compilation of high-pressure melting experiments. The steepest descent method and Monte Carlo sampling are combined to constrain all model parameters simultaneously instead of determining each parameter sequentially from relevant experiments. Our approach is applied to the published melting experiments on mantle materials to obtain the thermodynamic parameters of the MgO-FeO-SiO₂ ternary system. Inversion with the subsets of experimental data is conducted as well to investigate the source of discrepancy among existing studies, and the key parameters are found to be the thermal expansivity of SiO₂ and the excess volume of mixing between MgO and SiO₂. Mixing between FeO and SiO₂ is only constrained with large uncertainty, which could also imply that oxides with low concentrations have minimal effects on melting. Constraining the thermodynamics of MgO and SiO₂ will be important for a better understanding of mantle melting at high pressures.

1. Introduction

Terrestrial planets as large as the Earth are generally believed to have experienced multiple episodes of global-scale melting during their formation history by accretionary impacts, the release of gravitational energy, and radiogenic heat (e.g., Warren, 1985; Stevenson, 1987; Halliday et al., 2001; Elkins-Tanton, 2012). The existence of a magma ocean on the early Earth, in particular, is proposed by a number of theoretical studies, and the whole mantle could have been molten after the so-called Moon-forming giant impact (e.g., Matsui & Abe, 1986; Tonks & Melosh, 1993; Canup & Asphaug, 2001; Nakajima & Stevenson, 2015). The mode of magma ocean solidification has strong influences on the subsequent evolution, including crustal formation and the distribution of volatiles and incompatible elements. A good understanding of the thermodynamics of mantle melting is thus essential when considering how the putative magma ocean could have solidified, but it remains controversial at high pressures.

Our understanding of mantle melting also affects the interpretation of geochemical data pertinent to a model of core formation. The abundance of siderophile elements in the mantle is considered to reflect the history of temperature, pressure, and oxidation state at the base of the magma ocean, and if early experimental studies on mantle melting (Zerr et al., 1998; Tronnes & Frost, 2002) are used, it would point to the possibility that the Earth's mantle became more oxidized with time (Wade & Wood, 2005). This is theoretically consistent with late-stage accreting bodies being more oxidized (Rubie et al., 2015). The study by Fiquet et al. (2010), however, indicates higher melting temperature than previous studies, and if this is the case, the progressive oxidation of the mantle may not be necessary to explain the abundance of siderophile elements. Moreover, the melting temperature of the mantle can be even higher if fractional crystallization occurs in a magma ocean. An accurate knowledge of mantle melting is thus important not only for solving the evolution of a magma ocean but also for creating models of core formation and planetary accretion.

Several melting curves of mantle materials have been suggested based on high-pressure melting experiments (e.g., Zerr & Bohler, 1993; Fischer & Campbell, 2010; Fiquet et al., 2010; Andrault et al., 2011, 2014; Deng & Lee, 2017). Recently, melting curves at lower-mantle pressures are suggested to have a smaller slope than previously thought, indicating that the solidification can start from the midmantle region (Mosenfelder et al., 2009). This contrasts with the conventional view that a magma ocean solidifies from the bottom

(e.g., Solomatov & Stevenson, 1993; Abe, 1997). The midmantle solidification can result in a long-lasting melt pond above the core-mantle boundary, and such a deep melt layer could have evolved into a “hidden” geochemical reservoir (Labrosse et al., 2007), influencing the long-term evolution of the mantle. A difficulty lies, however, in evaluating consistency among different melting experiments. Disparity among reported melting temperatures has often been attributed to the presence of minor elements in starting materials, but the effect of minor elements remains uncertain.

Constructing a self-consistent thermodynamic model is one way of making progress toward a better understanding of mantle melting at high pressures. In a lower pressure range, studies since the 1980s have established reliable models for silicate systems (e.g., MELTS and THERMOCALC; Ghiorso et al., 1983, 2002; Berman & Brown, 1984; Holland & Powell, 1998). In these studies, standard-state chemical potentials are first determined for end-member components, followed by the estimation of their mixing properties. This sequential approach, however, is not directly applicable to a high-pressure range because a sufficient number of experimental data do not even exist to constrain end-members. For example, the melting temperature of MgO was debated until recently in the range of 5,000 to 8,000 K at the core-mantle boundary (Zerr & Bohler, 1993; Cohen & Gong, 1994; Alfè, 2005). For the MgO-SiO₂ binary system, only first-principle calculations exist (de Koker & Stixrude, 2009; de Koker et al., 2013). Other end-members and binary systems also suffer from similar situations.

In this study, we propose a new inversion scheme to determine all parameters regarding both end-members and mixing simultaneously, using a compilation of high-pressure melting experiments, which is applied to create a model of the MgO-FeO-SiO₂ ternary system. Over 90 wt% of the Earth's mantle is composed of these three components, and understanding this ternary system is a major step toward a more comprehensive model. Some of the parameters have already been estimated in existing studies, but results from experiments and molecular dynamic simulations are often associated with large uncertainties at high pressures. Therefore, instead of adopting existing estimates, all parameters are determined from our inversion scheme in an internally consistent manner. This will enable us to investigate how well melting experiments alone can constrain thermodynamic parameters. We will apply our method to the entire data set as well as some subsets of the data set, to better understand the origin of discrepancies among existing studies. Our inversion scheme fully quantifies the uncertainties of thermodynamic parameters, which can be used to identify any inconsistency among experiments. The paper is organized as follows. We first describe the formulation of chemical potentials adopted for liquid end-members. The formulation of our inversion scheme then follows. The estimated thermodynamic parameters are presented, with the corresponding phase diagrams and density profiles of mantle materials. Differences between our results and relevant previous studies (e.g., Andrault et al., 2011; Nomura et al., 2011; Boukaré et al., 2015) are also discussed. In our companion paper (Miyazaki & Korenaga, 2019), we will employ the obtained set of thermodynamic parameters to investigate the evolution of a magma ocean. When modeling a solidifying magma ocean where a liquid composition could evolve with possible chemical stratification, the use of such a self-consistent thermodynamic database will become essential.

2. Method

Our approach is to estimate thermodynamic parameters by comparing predicted melting temperatures directly with the results of multicomponent melting experiments. When calculating a melting temperature based on a thermodynamic model, the Gibbs free-energy minimization is required, which means that melting temperatures cannot be described as an explicit function of thermodynamic parameters. We employ a Monte Carlo method to constrain acceptable ranges of thermodynamic parameters. The results of the Monte Carlo sampling can be used to compute the mean and covariance of thermodynamic parameters.

In this study, we apply our method to determine the Gibbs free energy of liquids in the MgO-FeO-SiO₂ ternary system, although this approach is applicable to liquid systems with more components. The free energy of the liquid ternary system is parameterized as a function of 14 thermodynamic constants, eight of which are related to end-member liquids and the rest of which are their mixing properties. Each set of parameters has its corresponding misfit between the modeled melting temperatures and the experimental ones, and our goal is to efficiently explore the parameter space that has small misfits. The detailed description of each step, including the calculation of melting temperatures, is given below.

Table 1
Melting Experiments Considered in This Study, With Pressures Denoting the Data Adopted for Our Inversion

Starting materials	Reference	Pressures (GPa)
MgO	Kimura et al. (2017) (Alfè, 2005)	21, 31, 45 (90, 135)
FeO	Fischer and Campbell (2010)	25, 38, 47, 56, 69, 77
MgO-FeO	Deng and Lee (2017)	50, 80
SiO ₂	Shen and Lazor (1995) (Usui & Tsuchiya, 2010)	22, 31, 36 (108, 145)
MgSiO ₃	Zerr and Boehler (1993)	27, 32, 42, 52, 62
Peridotite	Fiquet et al. (2010)	Solidus: 36, 52, 80, 107, 122 Liquidus: 36, 61, 95, 139
Chondritic PM	Andrault et al. (2011)	Solidus: 34, 62, 82, 108, 140 Liquidus: 42, 70, 85, 110, 141

Note. Pressures in the parentheses denote molecular dynamics simulations. The melting curves of MgO and FeO are used to specify the melting temperature T_m in equation (2), whereas the others are adopted to evaluate the cost function (equation (14)). When modeling the melting temperatures of peridotite and chondritic primitive mantle (PM), the effects of trace elements are ignored, and the ternary compositions of MgO: 44.6 wt%, FeO: 7.8 wt%, and SiO₂: 47.5 wt% and MgO: 37.7 wt%, FeO: 9.1 wt%, and SiO₂: 53.2 wt% are used instead.

2.1. Gibbs Free Energy of the Ternary System

We first describe the formulation of the Gibbs free energy of the MgO-FeO-SiO₂ ternary system. For solid components, the published database by Stixrude and Lithgow-Bertelloni (2011) is employed to describe their chemical potentials. This study focuses on melting under lower mantle conditions, so bridgmanite and ferropericlase are considered for Mg- and Fe-bearing species and stishovite and seriferfite for pure SiO₂ species. Liquid in this system is represented as a mixture of three end-member components, MgO, FeO, and SiO₂, and the nonideal contribution of their mixing is described using a regular symmetric solution model. The chemical potential of end-member liquid component i , μ_i^l , is given by

$$\mu_i^l = \mu_i^{l,0} + RT \log(\gamma_i x_i^l), \quad (1)$$

where the superscript 0 denotes standard state, R is the universal gas constant, T is absolute temperature, and x_i^l and γ_i , respectively, denote the molar ratio and activity coefficient of component i in the liquid phase. We aim to parameterize standard-state chemical potentials, $\mu_i^{l,0}$, with a minimum number of parameters because only a limited number of experiments are currently available.

For MgO and FeO liquids, the standard-state chemical potentials are constructed with reference to those of corresponding solids. The chemical potential of liquid, μ_i^l , is set to be equal to that of corresponding solid, μ_i^s , at melting temperature, T_m . Melting temperature is obtained from experiments listed in Table 1. Melting temperatures in between the measurements are interpolated using cubic spline. By integration of the entropy change upon melting, ΔS_i , the chemical potential of liquid component i at any given temperature can be calculated as

$$\mu_i^{l,0}(T, P) = \mu_i^s(T, P) + \int_{T_m}^T \Delta S_i dT'. \quad (2)$$

The entropy change upon melting is usually a weak function of temperature (e.g., JANAF Thermochemical Table), and therefore, it may be parametrized as a function of pressure only:

$$\Delta S_i = \Delta S_i^0 \left(1 - A_i \left(1 - \exp \left(-\frac{P}{P_1} \right) \right) \right). \quad (3)$$

This equation assumes that the entropy change upon melting decreases exponentially with increasing pressure, where the extent of decrease at P_1 is described by A_i . The entropy change at ambient pressure, ΔS_i^0 , is set to 25.1 JK⁻¹ mol⁻¹ for MgO and 14.6 JK⁻¹ mol⁻¹ for FeO, which are taken from JANAF Thermodynamic

Table. By combining equations (2) and (3) and by assuming the melting temperature at each pressure, the standard-state chemical potential can be expressed using the single parameter A_i .

This approach, however, is not suitable for parameterizing the chemical potential of SiO_2 liquid. Because the solid of SiO_2 experiences multiple phase changes, formulating the entropy change upon melting becomes cumbersome if we aim to maintain the continuity of the chemical potential of liquid over the entire pressure range under consideration. The number of parameters necessary to describe the potential would also increase, diminishing the advantage of this approach. For SiO_2 liquid, therefore, we define a single reference point in the entire temperature-pressure space, and the standard-state chemical potential is calculated by sequentially integrating along a path of constant pressure and that of constant temperature:

$$\mu_{\text{SiO}_2}^{l,0}(T, P) = \mu_{\text{SiO}_2}^{l,0}(T_{m,0}, P_{\text{atm}}) + \int_{P_{\text{atm}}}^P V(T_{m,0}, P') dP' - \int_{T_{m,0}}^T S(T', P) dT', \quad (4)$$

where V is molar volume, S is molar entropy, and $T_{m,0}$ is the melting temperature of quartz at the ambient pressure, P_{atm} . As a reference point, $T_{m,0}$ and P_{atm} are used, and the liquid chemical potential at this point is set to match the chemical potential of quartz. Molar volume at the reference temperature $V(T_{m,0}, P)$ is described with the Murnaghan equation of state (Murnaghan, 1951) as

$$V(T_{m,0}, P) = V_0 \left(1 + K'_0 \frac{P}{K_0} \right)^{-1/K'_0}, \quad (5)$$

where K_0 denotes the bulk modulus, and K'_0 is its pressure derivative. The reference molar volume, V_0 , is taken to match the molar volume at the reference point. Entropy is obtained by integrating its temperature and pressure derivatives:

$$S(T, P) = S_0 + \int_{T_{m,0}}^T \frac{C_0 + C_1(T' - T_0)^n}{T'} dT' - \int_{P_{\text{atm}}}^P \alpha V(T, P') dP', \quad (6)$$

where S_0 is the entropy at the reference point, which is taken from the JANAF database. The numerator of the second term on the right-hand side represents heat capacity, which is assumed to increase exponentially with temperature. Heat capacity is described using three parameters: the reference value, C_0 , its temperature dependence, C_1 , and the exponent, n . A theoretical study has suggested that the exponent may be negative with a value of $n = -0.4$ for dense, simple liquid (Rosenfeld & Tarazona, 1998), but first principle calculations indicate that such a relation does not hold for most melt of mantle-composing minerals (de Koker & Stixrude, 2009). For simplicity, some previous studies have assumed a linear model (Boukaré et al., 2015), although the temperature dependence of heat capacity is likely to become smaller at higher temperatures. In this study, we will test two different values of n , 0.5 and 1. Thermal expansivity, α , changes with pressure as

$$\alpha = \alpha_0 \exp\left(-\frac{\delta_T}{K_0} P\right), \quad (7)$$

where δ_T denotes the Anderson-Grüneisen parameter. This equation assumes that δ_T is independent of temperature and pressure, which is valid at least for solids (Anderson, 1995). Equations (4)–(7) fully describe the standard-state chemical potential of SiO_2 liquid.

Lastly, the activity coefficients are described with the Margules parameters (Helfrich & Wood, 1989) as

$$RT \log \gamma_{\text{MgO}} = \left((1 - x_{\text{MgO}}^l) W^{\text{Mg-Si}} - x_{\text{FeO}}^l W^{\text{Fe-Si}} \right) x_{\text{SiO}_2}^l, \quad (8)$$

$$RT \log \gamma_{\text{FeO}} = \left((1 - x_{\text{FeO}}^l) W^{\text{Fe-Si}} - x_{\text{Mg}}^l W^{\text{Mg-Si}} \right) x_{\text{SiO}_2}^l, \quad (9)$$

$$RT \log \gamma_{\text{SiO}_2} = \left(x_{\text{MgO}}^l W^{\text{Mg-Si}} + x_{\text{FeO}}^l W^{\text{Fe-Si}} \right) \left(x_{\text{MgO}}^l + x_{\text{FeO}}^l \right), \quad (10)$$

where $W^{\text{Mg-Si}}$ and $W^{\text{Fe-Si}}$ denote the Margules parameter for the MgO-SiO_2 and the FeO-SiO_2 binary systems, respectively. Here MgO-FeO liquid is considered to mix ideally, so the Margules parameter for the MgO-FeO binary system is zero. Assuming linear dependence on temperature and pressure, each Margules parameter can be parameterized as a function of three constants,

$$W^i = W_0^i + V_0^i(P - P_{\text{ref}}) - S_0^i(T - T_{\text{ref}}), \quad (11)$$

where P_{ref} and T_{ref} denote the reference pressure and temperature, respectively. We set P_{ref} to P_{atm} and T_{ref} to 1,500 K. The excess volume and entropy of mixing correspond to V_0^i and S_0^i , respectively.

To summarize, we adopt a total of 14 parameters to describe the Gibbs free energy of the ternary system. For MgO and FeO end-member components, two A_i s are used to describe the pressure dependence of entropy change upon melting. Six parameters are used for SiO₂, including bulk modulus K_0 , its pressure derivative K'_0 , thermal expansivity α_0 , heat capacity C_0 , its temperature dependence C_1 , and Grüneisen-Anderson parameter δ_0 . Six additional parameters are employed to describe the mixing of MgO-SiO₂ and FeO-SiO₂ binary systems. These 14 parameters will be determined by Monte Carlo sampling.

2.2. Monte Carlo Sampling

In order to constrain the model parameters, we aim to collect an ensemble of parameters that yield acceptable fits to the data using a Monte Carlo approach. We first create a series of randomized data, where i th data point, T_{exp}^i , is drawn from the normal distribution with its mean equal to an experimentally determined temperature and the standard deviation of experimental uncertainty, σ^i . The Mersenne Twister (Matsumoto & Nishimura, 1998) is used as a pseudorandom number generator. For each randomized data set, best-fit model parameters are calculated, and the results of the optimization are gathered to estimate the mean and covariance of the parameters as follows:

$$\bar{x} \approx \frac{1}{N} \sum_{i=1}^N x_i, \quad (12)$$

$$\text{cov}(x, y) \approx \frac{1}{N} \sum_{i=1}^N (x_i - \bar{x})(y_i - \bar{y}), \quad (13)$$

where x_i and y_i denote the i th Monte Carlo solution of the model parameters x and y , and N the total number of randomized data sets.

The cost function, χ^2 , quantifies a misfit between model predictions and experimental data, which is minimized using the steepest descent method. The cost function is defined as

$$\chi^2 = \sum_i \left(\frac{T_{\text{calc}}^i - T_{\text{exp}}^i}{\sigma^i} \right)^2, \quad (14)$$

where T_{calc}^i denotes modeled temperature. The data sets employed in this study are summarized in Table 1. A similar number of data points is chosen from each experiment to avoid being biased toward a particular experiment. Data are also selected so that pressure intervals between them are roughly the same. For end-member components, data points are added near the core-mantle-boundary pressure by referring to the molecular dynamics simulations (Alfè, 2005; Usui & Tsuchiya, 2010) in order to reduce the uncertainties at high pressure.

Before starting the minimization, all 14 parameters are first normalized on the order of unity. We start the minimization from values chosen randomly from the ranges listed in Table 2, which are chosen to include previous estimates. The gradient, g_k , is then calculated numerically by perturbing each normalized parameter for 10^{-3} at each iteration. The normalized parameters, n_k , are updated using the recurrence:

$$n_{k+1} = n_k - \alpha_k g_k, \quad (15)$$

where a positive step size α_k is determined by a golden section search. If necessary, the step size α_k will be adjusted to satisfy the a priori constraint. A priori constraint is defined for each parameter to ensure that values are physically plausible.

2.3. Calculating Melting Temperature

Melting temperatures are calculated based on the Gibbs free-energy minimization method described in Miyazaki and Korenaga (2017). To make it more computationally efficient, it is here combined with a reaction-based approach, in which we search for a temperature that the chemical potentials of solid and liquid phases are identical. For the melting of a single mineral, chemical potentials of liquid and solid phases are simply compared because the chemical potentials of the reactant and product of melting reactions are equivalent at the melting temperature. For SiO₂, the solid phase corresponds to stishovite or seifertite and

Table 2
Model Parameters Obtained From the Inversion of Melting Experiments

	For the steepest descent method			$n = 1$	$n = 1$ (without chondritic PM)	$n = 0.5$ (without chondritic PM)	Previous estimates
	A	B	C	(all data)			
A_{MgO}	1	[0.5, 1]	$(-\infty, 1]$	0.90 ± 0.03	0.96 ± 0.04	0.93 ± 0.04	—
A_{FeO}	1	[-1, 1]	$(-\infty, 1]$	-0.52 ± 0.20	-0.38 ± 0.33	-0.47 ± 0.29	—
K_0 (GPa)	20	[15, 35]	$[0, \infty)$	26.7 ± 2.60	26.2 ± 2.55	26.1 ± 2.09	$16.24^a, 7.1^b$
K'_0	1	[3, 5]	$[0, \infty)$	4.16 ± 0.24	4.25 ± 0.24	4.21 ± 0.27	$3.92^a, 17.1^b$
α_0 (10^{-6} K^{-1})	20	[5, 45]	$[0.1, 10]$	7.15 ± 1.92	15.4 ± 2.22	15.0 ± 2.81	$47^a, 121^c$ $12.3\text{--}123^b$
C_0 (JK^{-1})	1	[1, 4]	$[0, \infty)$	2.49 ± 1.93	3.32 ± 1.94	13.6 ± 2.01	—
C_1 ($10^{-2} \text{ J K}^{-n-1}$)	1	[5, 7]	$[0.1, 10]$	5.49 ± 0.11	5.59 ± 0.13	200 ± 2.01	—
δ_0	1	[0, 10]	$[0, \infty)$	0.66 ± 0.36	0.24 ± 0.36	2.14 ± 0.46	—
$W_0^{\text{Mg-Si}}$ (kJ mol^{-1})	200	[-200, 200]	$(-\infty, \infty)$	-122 ± 18.0	-127 ± 14.7	-119 ± 16.6	-126.8^a
$v_0^{\text{Mg-Si}}$ ($\text{cm}^3 \text{ mol}^{-1}$)	1	[0, 3]	$(-\infty, \infty)$	0.31 ± 0.13	1.31 ± 0.10	1.33 ± 0.11	0.088^a
$s_0^{\text{Mg-Si}}$ ($\text{JK}^{-1} \text{ mol}^{-1}$)	10	[0, 30]	$(-\infty, \infty)$	-1.2 ± 10.7	3.4 ± 10.0	2.0 ± 9.33	30^a
$W_0^{\text{Fe-Si}}$ (kJ mol^{-1})	2000	[-200, 200]	$(-\infty, \infty)$	-170 ± 45	-100 ± 114	-125 ± 87	-49.1^a
$v_0^{\text{Fe-Si}}$ ($\text{cm}^3 \text{ mol}^{-1}$)	10	[0, 3]	$(-\infty, \infty)$	1.75 ± 1.05	0.47 ± 2.94	0.72 ± 3.55	0.19^a
$s_0^{\text{Fe-Si}}$ ($\text{JK}^{-1} \text{ mol}^{-1}$)	100	[0, 30]	$(-\infty, \infty)$	3.6 ± 34.0	53.0 ± 26.5	30.2 ± 21.3	0^a
$\chi^2_{\text{min}}/N_{\text{data}}$				3.07	0.81	0.88	

Note. The mean values and one standard deviations of model parameters are reported for three separate Monte Carlo samplings. The first case shows the result of the inversion on the entire data set shown in Table 1, whereas the latter two cases employ the data set excluding chondritic primitive mantle (PM) using two values for the exponent of n in equation (6). Normalizing constants, ranges of initial values, and a priori bounds used in the steepest descent method are listed as well. A = normalizing constants, B = ranges of initial values, and C = a priori bounds.

^aBoukaré et al. (2015). ^bDingwell et al. (1993). ^cde Koker and Stixrude (2009).

the liquid phase to the melt of SiO_2 . For MgSiO_3 , the solid phase is represented by Mg-bridgmanite, and the liquid phase is described as the mixture of MgO and SiO_2 melts.

For the solidus and liquidus temperatures of a solid solution, we make use of the fact that only an infinitesimal amount of liquid and the solid, respectively, is present. For the MgO-FeO binary system, for example, the following two equations have to be satisfied simultaneously:

$$\begin{aligned} \mu_{\text{MgO}}^{s,0}(T) + RT \log(x_{\text{MgO}}^s) &= \mu_{\text{MgO}}^{l,0}(T) + RT \log(x_{\text{MgO}}^l) \\ \mu_{\text{FeO}}^{s,0}(T) + RT \log(x_{\text{FeO}}^s) &= \mu_{\text{FeO}}^{l,0}(T) + RT \log(x_{\text{FeO}}^l), \end{aligned} \quad (16)$$

where x_i^s denotes the molar ratio of solid component i . At the solidus, the solid contains virtually all of the mass, so x^s can be represented by the equilibrium composition without the presence of liquid. Equation (16) can thus be solved for T , x_{MgO}^l , and x_{FeO}^l under $x_{\text{MgO}}^l + x_{\text{FeO}}^l = 1$. Likewise, the liquidus temperature can be calculated by solving for T , x_{MgO}^s , and x_{FeO}^s , assuming that liquid composition x^l carries the bulk composition.

The sequence of equilibrium phases between the solidus and liquidus, which is calculated using Gibbs free-energy minimization, shows that melt fraction changes continuously from 0 to 1 for mantle compositions (Figure 1a). This indicates that the same approach with the binary system can be used to calculate the solidus and liquidus temperatures of our ternary mantle system. At solidus, the solid of bulk composition is in equilibrium with an infinitesimal amount of melt. To calculate the melting temperatures of our ternary mantle system, the following equations are solved simultaneously:

$$\begin{aligned} \mu_{\text{MgSiO}_3}^{s,0}(T) + RT \log(x_{\text{Mg}}^{\text{br}}) &= \mu_{\text{MgO}}^{l,0}(T) + RT \log(\gamma_{\text{MgO}} x_{\text{MgO}}^l) + \mu_{\text{SiO}_2}^{l,0}(T) + RT \log(\gamma_{\text{SiO}_2} x_{\text{SiO}_2}^l) \\ \mu_{\text{FeSiO}_3}^{s,0}(T) + RT \log(x_{\text{Fe}}^{\text{br}}) &= \mu_{\text{FeO}}^{l,0}(T) + RT \log(\gamma_{\text{FeO}} x_{\text{FeO}}^l) + \mu_{\text{SiO}_2}^{l,0}(T) + RT \log(\gamma_{\text{SiO}_2} x_{\text{SiO}_2}^l) \\ \mu_{\text{MgO}}^{s,0}(T) + RT \log(x_{\text{MgO}}^{\text{pe}}) &= \mu_{\text{MgO}}^{l,0}(T) + RT \log(\gamma_{\text{MgO}} x_{\text{MgO}}^l), \end{aligned} \quad (17)$$

where x_{Mg}^j and x_{Fe}^j are the molar ratio of Mg and Fe end-members, respectively, in phase j , and the superscripts pe and br denote ferropericlase and bridgmanite, respectively. For the solidus, T and x_i^l are solved

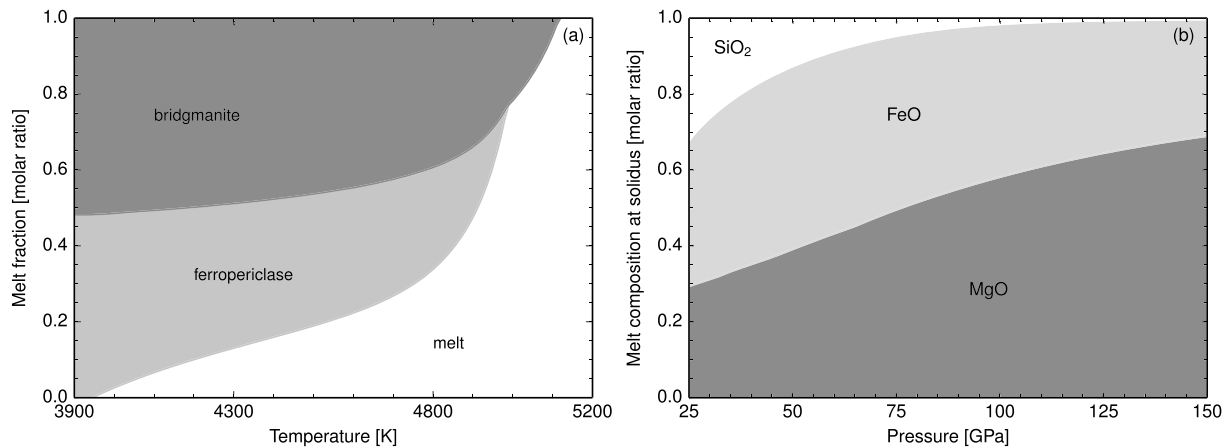


Figure 1. (a) The sequence of equilibrium phases between the solidus and liquidus temperatures for peridotite at 100 GPa. Results are calculated using the parameters that are obtained from the data set without chondritic primitive mantle, with $n = 1$ as an exponent of heat capacity. With increasing temperature, ferropericlasite (gray) disappears first, whereas bridgmanite (black) remains present until the liquidus. Melt fraction changes continuously with temperature. (b) The composition of melt emerging at the solidus temperature for the case of peridotite, calculated with the model parameters that are used to generate the synthetic data set. As pressure increases, MgO (black) dominates the melt, whereas the amount of FeO (gray) becomes negligible. The silica content (white) remains roughly the same.

under $x_{\text{MgO}}^l + x_{\text{FeO}}^l + x_{\text{SiO}_2}^l = 1$, and the solid composition x_i^s is the equilibrium compositions of ferropericlasite x^{pe} and bridgmanite x^{br} without the presence of melt, which can be solved using the Gibbs free-energy minimization. Instead of solving for the four unknowns simultaneously, equation (17) is first solved for x_{MgO}^l , x_{FeO}^l , and $x_{\text{SiO}_2}^l$ for a range of T using the Newton-Raphson method, and then the temperature that satisfies $x_{\text{MgO}}^l + x_{\text{FeO}}^l + x_{\text{SiO}_2}^l = 1$ is chosen as the solidus.

Whether or not the system melts gradually can be predicted using the Gibbs' phase rule. For example, the MgO-SiO₂ binary system involves three equilibrium phases (bridgmanite, periclasite, and melt) at solidus, indicating that it has zero degree of freedom under constant pressure. As a result, either bridgmanite or periclasite has to melt completely at the solidus temperature, and the amount of melt increases discontinuously across solidus. On the other hand, our mantle ternary system involves the same number of phases at solidus with the binary system, yet the system includes iron in addition to Mg, Si, and O. This creates an additional degree of freedom, which allows the melt fraction of the system to change gradually.

At the liquidus, the melt will carry the bulk of the total mass, and a trace amount of bridgmanite exists in the solid phase, which is also observed experimentally (Fiquet et al., 2010). The liquidus temperature can thus be solved using the first equation of (17), which represents the melting reaction of bridgmanite. The fraction of Mg component in bridgmanite $x_{\text{Mg}}^{\text{br}}$ is set to 1, whereas x_i^l carries the bulk composition. As bridgmanite may not necessarily be the liquidus phase for some sets of thermodynamic parameters, Gibbs free-energy minimization is conducted at every 100 steps of the steepest descent method to ensure that the considered phases are correct.

3. Recovery Test With a Synthetic Data Set

We first apply this approach to a synthetic data set to demonstrate its validity. The data set is created to resemble the experiments listed in Table 1 so that the uncertainties of parameters associated with the scarcity of data can be reflected as well. Data points are generated using Gibbs free-energy minimization at similar pressures and compositions with the experiments. We repeat the Monte Carlo sampling until the median and standard deviation of all distributions are reasonably well defined, which is usually achieved by $\sim 2,000$ iterations.

Melting curves calculated from the recovered model parameters show a good agreement with the input data (Figure 2). Uncertainties become larger at higher pressures for all melting curves because of the small number of data, although the solidus temperatures below 40 GPa are also associated with large uncertainties. Because a linear relationship between pressure and the Margules parameters is assumed, the uncertainties in the higher pressure propagate to the lower pressure range. With our approach, the Margules parameters

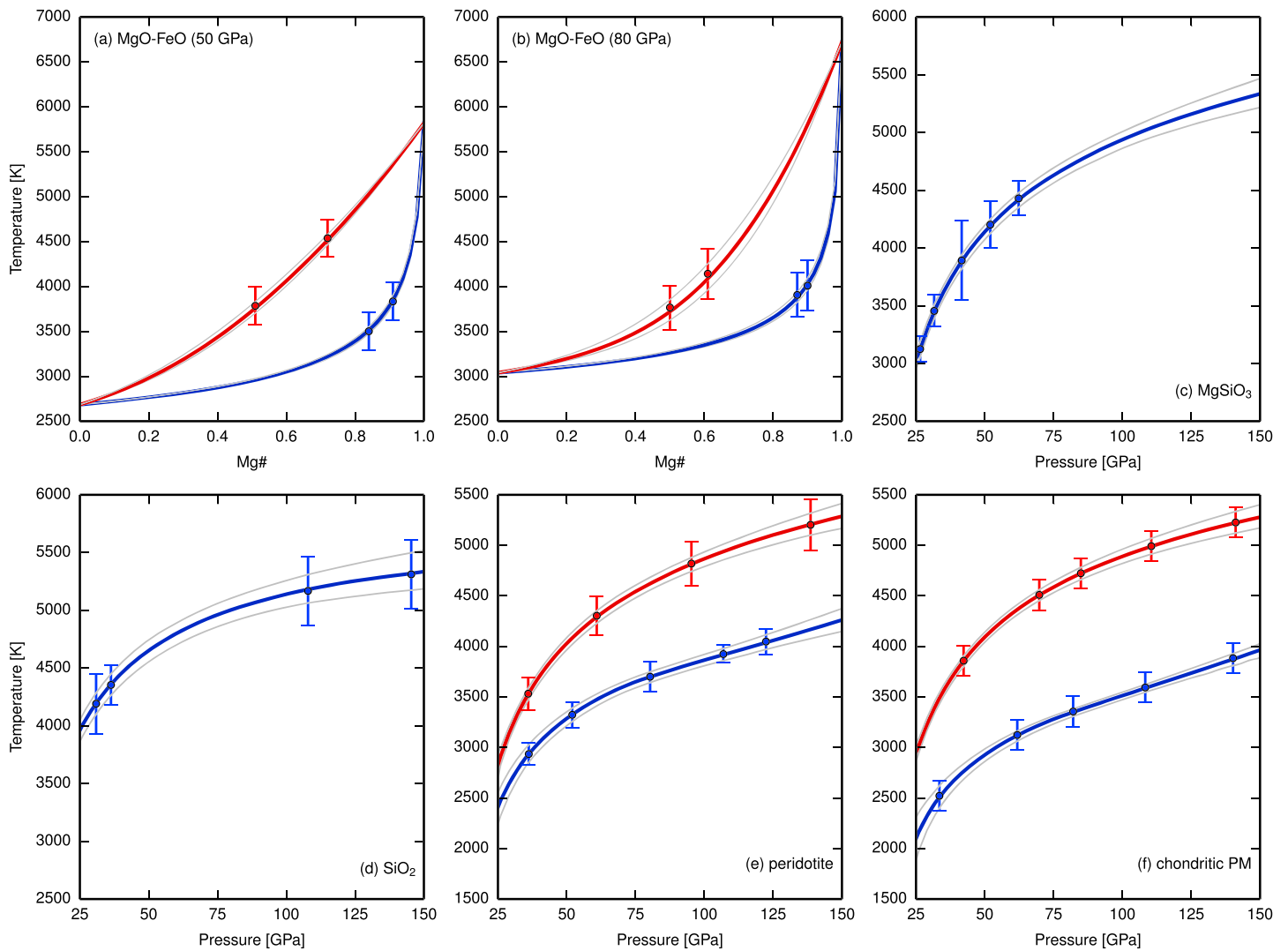


Figure 2. Comparison of synthetically generated input data (circle) and recovered melting curves (solid line) for (a) the MgO-FeO binary system at 50 GPa, (b) the same system at 80 GPa, (c) MgSiO₃, (d) SiO₂, (e) peridotite, and (f) chondritic primitive mantle (PM). A series of melting curves are calculated using solutions from Monte Carlo sampling, and their median (thick line) and 95 % confidence interval (thin gray) are shown. Both solidus (blue) and liquidus (red) temperatures are shown in (a), (b), (e), and (f). The melting temperatures of FeSiO₃ are reproduced within the uncertainties as well.

at midmantle pressures are thus determined with the smallest uncertainty in order to minimize the misfit of the entire data set.

All parameters are successfully reproduced within one standard deviation from the mean value (Figure 3). The a posteriori probability distributions of C_1 and $v_0^{\text{Mg-Si}}$ exhibit small uncertainties compared to the range of physically plausible value, whereas parameters associated with FeO are only loosely constrained. The melting curves can be reproduced within the uncertainties of the measurement even when the mixing reaction between FeO and SiO₂ is exothermic ($W_0^{\text{Fe-Si}} > 0$), meaning that these parameters have only small contributions to determining the melting temperatures of mantle materials. This can be explained by two factors: (1) the small iron content and (2) the near-complete melting of FeO below the liquidus temperature. The liquidus temperature is determined mostly by the melting of Mg-bridgmanite to MgO and SiO₂ liquids, so their activity coefficients are the key controlling factors. Because of the small iron content, however, these coefficients include only a small contribution from the Margules parameter for the FeO-SiO₂ system ($W^{\text{Fe-Si}}$). Therefore, the liquidus temperature becomes insensitive to the mixing parameters between FeO and SiO₂. The effects of other oxides are also likely to be insignificant if the concentration is small enough and the oxides are completely melted below liquidus. Mg-bridgmanite is indeed observed as the last stable phase

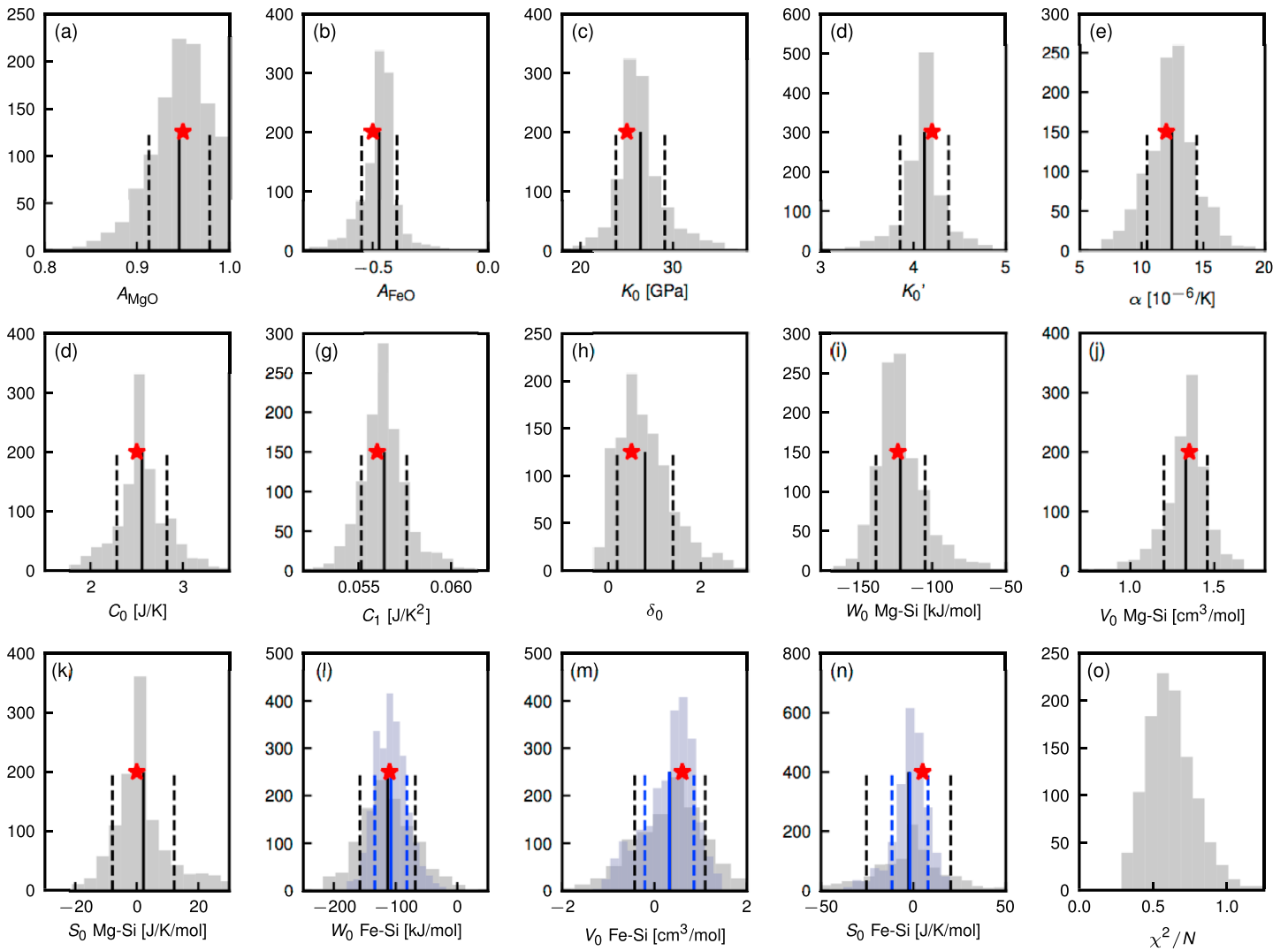


Figure 3. The histogram of recovered model parameters obtained from 2,000 Monte Carlo solutions to the synthetically generated data. For heat capacity, $n = 1$ is assumed here (equation (6)). (a, b) Pressure dependence of entropy change upon melting (a) for MgO and (b) for FeO. (c–f) Bulk modulus, its pressure derivative, thermal expansivity, heat capacity at the reference temperature, temperature derivative of heat capacity, and Grüneisen-Anderson parameter of SiO₂ liquid, respectively. (i) Margules parameter at the reference temperature, (j) excess volume, and (k) excess entropy for the mixing between MgO and SiO₂. (l–n) The same with (i)–(k) but for the mixing between FeO and SiO₂. (o) The normalized cost function. The mean (solid) and one standard deviation about the mean (dash) are marked with lines, whereas the original values used to create the synthetic data are shown with red stars. In (l)–(n), histograms based on the data set including FeSiO₃ solidus are also plotted in blue.

in the experiment (Fiquet et al., 2010), which validates the assumption of neglecting other oxides. When the melting temperature of an oxide is higher than MgO or lower than FeO, however, the last stable phase may not be bridgmanite, and therefore, its effect cannot be ignored. Furthermore, the melt emerging at the solidus contains only a small amount of silica at high pressures (Figure 1b). When the silica content of melt is negligible ($x_{\text{SiO}_2}^l \approx 0$), the melting is mostly determined by the mixing between MgO and FeO, so the mixing between FeO and SiO₂ has a minimal effect on the solidus temperature as well.

Although the melting temperatures of mantle compositions are not largely affected by the mixing between FeO and SiO₂, its effect becomes important when considering a composition enriched in iron, including the liquid phase in the final phase of magma ocean solidification. In order to investigate how the mixing parameters will be constrained with additional experimental data, we generated more data points for the solidus temperatures of FeSiO₃ composition at 30, 50, 70, 90, and 110 GPa. When the same recovery test is conducted with these new data, uncertainties for $W_0^{\text{Fe-Si}}$, $V_0^{\text{Fe-Si}}$, and $S_0^{\text{Fe-Si}}$ are reduced by 45%, 35%, and 50%,

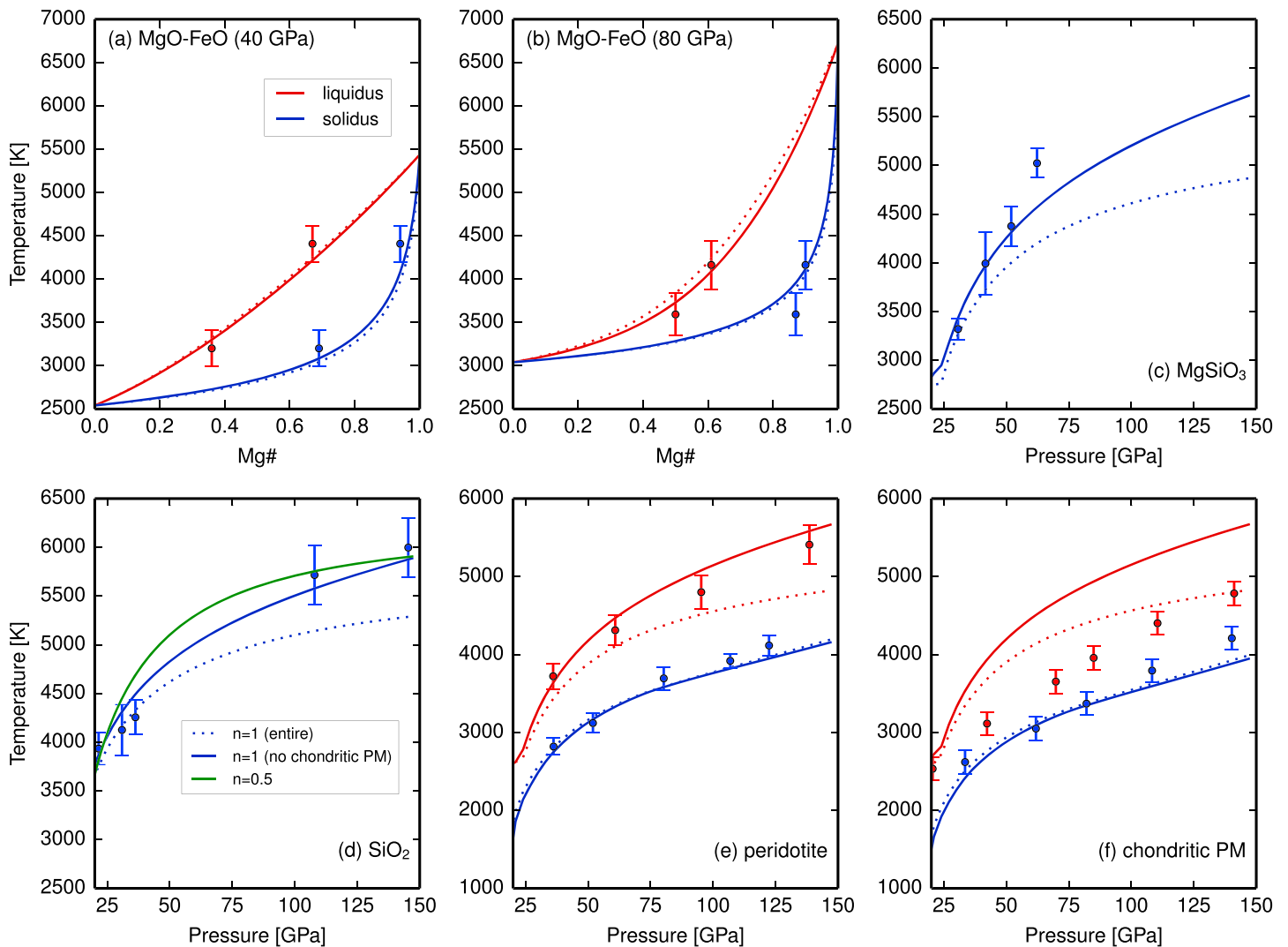


Figure 4. Comparison of predicted melting curves and experimental data (circle) for (a) the MgO-FeO binary system at 40 GPa, (b) the same system at 80 GPa, (c) MgSiO₃, (d) SiO₂, (e) peridotite, and (f) chondritic primitive mantle (PM). Both solidus (blue) and liquidus (red) temperatures are shown in (a), (b), (e), and (f). The parameters determined from the inversion on the entire data set listed in Table 1 (dotted) are used to predict the melting curves as well as the ones determined from the inversion using the one excluding chondritic PM (solid). The exponent of $n = 1$ is assumed in equation (6) (i.e., the heat capacity of SiO₂ increases linearly with temperature) to predict the melting temperature. For SiO₂, the melting curve assuming $n = 0.5$ is also shown as well (green).

respectively. Note that its liquidus temperature does not help constrain these parameters, again, because FeO melts completely below liquidus, and stishovite is the last solid phase to remain.

4. Results

The method to constrain the thermodynamic model parameters is now applied to the data from the melting experiments listed in Table 1. The melting experiments of MgO and FeO are used to specify the melting temperature T_m in equation (2), whereas the rest of the data are used in equation (14) to evaluate the cost function. For the experiments on mantle materials, compositions are first projected to the MgO-FeO-SiO₂ ternary system. As discussed in section 3, the existence of other oxides including Al₂O₃ and CaO is unlikely to cause a substantial change in melting temperature given that their concentrations are lower than iron.

When our method is applied to the entire data set, the value of normalized cost function (i.e., χ^2/N_{data} where N_{data} is the number of data points) does not fall below ~ 3 . This indicates that modeled temperatures are, on average, out of three standard deviations of experimental observations. As seen in Figure 4, the model predictions deviate significantly from experiments for the melting temperatures of MgSiO₃, SiO₂, and the

mantle liquidus at high pressure. Such discrepancy between the model predictions and the experiments may be caused by an insufficient number of model parameters used to describe the liquid, but inversions will likely become more poorly constrained with the current size of the data set if more degrees of freedom are introduced.

Another possible explanation for the discrepancy is inconsistency among experimental data. The observed liquidus temperatures of peridotite and chondritic primitive mantle (PM) differ by ~ 800 K, despite having a similar composition. To assess the plausibility of this hypothesis, our method is also applied to the subsets of the data set. We consider two subsets that do not include the experiments on peridotite and chondritic PM. In the former case, the predicted melting temperatures for all materials become even lower to account for low mantle liquidus temperatures. Fit to experimental data does not improve, and the normalized cost function remains above 3. For the data set without chondritic PM, on the other hand, the normalized cost function reaches below ~ 0.8 , indicating that the experimental data are explained by the model within one standard deviation. Indeed, all data points other than that of MgSiO_3 at 61 GPa are reasonably well explained (Figure 4).

The estimated means and standard deviations of model parameters are summarized in Table 2. A set of parameters that can reproduce the entire data within uncertainty is not found, so the one that minimizes the misfit is shown for comparison. The results for the entire data set are in fact in good agreement with those obtained from the one excluding chondritic PM, except for α_0 and $v_0^{\text{Mg-Si}}$. The estimates of these two parameters are nonoverlapping, where smaller values are predicted for the former case compared to the latter. This suggests that these two parameters are chiefly responsible for the difference in the melting temperatures of SiO_2 and the mantle liquidus (Figures 4c, 4e, and 4f).

The parameter $v_0^{\text{Mg-Si}}$ controls the degree of nonideal mixing at high pressure and thus creates a difference in the mantle liquidus, whereas the large uncertainties observed in parameters describing the mixing between FeO and SiO_2 have minimal effects on the melting temperatures as discussed in section 3. Among all the mixing parameters, the estimates of $W_0^{\text{Mg-Si}}$ and $W_0^{\text{Fe-Si}}$ show a good agreement with the values used in Boukaré et al. (2015), which is compatible with the fact that the mixing at ambient conditions is well constrained. On the other hand, their adopted value of $v_0^{\text{Mg-Si}}$ is smaller than our estimate. The liquidus temperature presented by Boukaré et al. (2015) is lower than our prediction, which is consistent with the relation that smaller $v_0^{\text{Mg-Si}}$ leads to lower liquidus temperature (Figure 4). When a data set without the experiments on peridotite is used, on the other hand, a negative $v_0^{\text{Mg-Si}}$ is suggested, which results in a even smaller liquidus temperature.

The other key parameter is the thermal expansivity of SiO_2 (α_0), which accounts for the difference in melting temperatures of SiO_2 . The estimates on α_0 , however, vary significantly among different studies (Hudon et al., 2002; de Koker & Stixrude, 2009), and our results of $\sim 10^{-5}$ is on the lower end of these estimates. We also tested a different expression for the heat capacity of SiO_2 to exclude the possibility that such difference is caused by the choice of parameterization. The estimate does not change much even when $n = 0.5$ is assumed in equation (6), indicating that small thermal expansivity is consistent with the current data set.

5. Discussion

5.1. Phase Diagram for the (Mg,Fe)O-SiO₂ System

Phase diagrams for the MgO-SiO_2 and $(\text{Mg}_{0.9}, \text{Fe}_{0.1})\text{O-SiO}_2$ systems based on the best-fit parameters show an eutectic feature (Figure 5). The two different values for the exponent in equation (6) change the eutectic composition only by $\sim 5\%$ at most, and the overall topology of phase diagrams remains identical. As pressure increases, the eutectic composition becomes more depleted in SiO_2 for both cases, which is more noticeable in the system with FeO, indicating that the liquidus phase for most mantle materials is likely to be bridgmanite for a wide range of SiO_2 content. Recent studies, however, suggest a eutectic melt composition with 38–40 mol% of SiO_2 , and they predict that the composition remains mostly unchanged with pressure (Liebske & Frost, 2012; de Koker et al., 2013; Boukaré et al., 2015).

To investigate this discrepancy, the dependence of the eutectic composition on thermodynamic parameters has been analyzed by calculating the eutectic for multiple sets of randomized parameters. A strong negative correlation is found between A_{MgO} and the eutectic composition, whereas other parameters show an order of magnitude weaker correlations (Figure 5e). By lowering the value of A_{MgO} (i.e., larger entropy change upon melting for MgO), a eutectic composition as high as 40 mol% of SiO_2 is indeed achievable while keeping other parameters the same, although the misfit between our compiled data set becomes larger. Most of the misfit

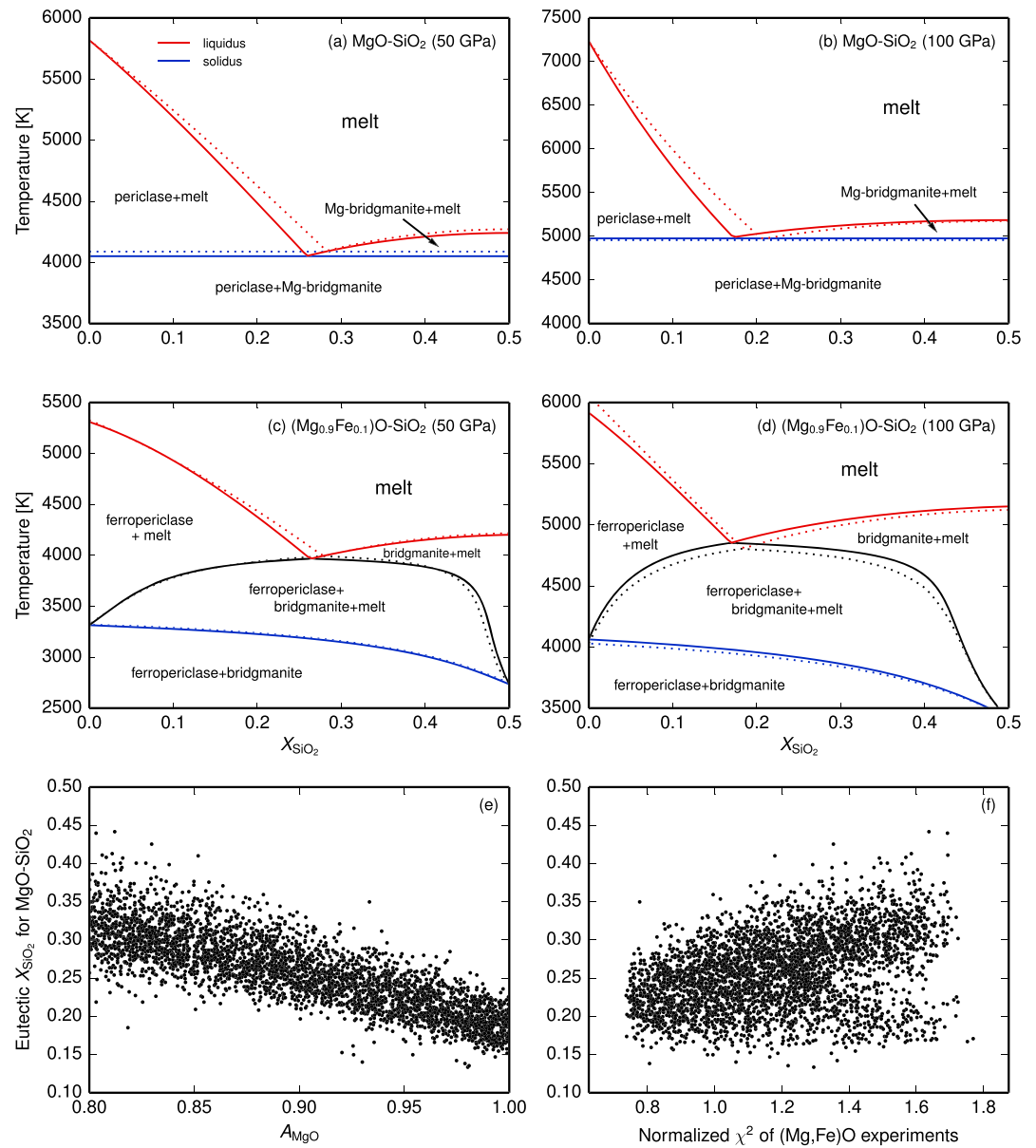


Figure 5. (a–d) Phase diagrams showing the binary joint of MgO-SiO₂ at (a) 50 and (b) 100 GPa and those of (Mg_{0.9}Fe_{0.1})O-SiO₂ at (c) 50 and (d) 100 GPa, using the parameters obtained from the data set without chondritic primitive mantle. Both cases of $n = 1$ (solid) and $n = 0.5$ (dotted) are shown for the exponent of heat capacity. Solidus (blue) and liquidus (red) are indicated by color. (e) Scatter plot for A_{MgO} and the SiO₂ content of the MgO-SiO₂ eutectic composition. Other thermodynamic parameters are randomly selected within two standard deviations of the mean from Table 2. Results of $n = 1$ from the data set without chondritic primitive mantle are used. (f) Same as (e) but, on x axis, normalized cost function (χ^2/N) for experiments on (Mg,Fe)O.

increase arises from disagreement with the experiments on (Mg, Fe)O by Deng and Lee (2017; Figure 5f), whereas the work of Deng and Lee (2017) has recently been corroborated by others (Fu et al., 2018). Thus, the low SiO₂ eutectic composition appears to be a natural consequence of the choice of experiments included in our data set.

For the case of (Mg_{0.9}, Fe_{0.1})O-SiO₂, solidus temperatures vary gradually with the SiO₂ content. Peridotite in Table 1 contains 10 mol% more Mg and 9 mol% less Si compared to chondritic PM, and such difference should result in a temperature difference of only ~150 K. This is consistent with the fact that the solidi of peridotite and chondritic PM show a good agreement with each other. Note that the melt does not completely solidify right beneath the cotectic temperature, and it takes another ~900 and ~700 K of cooling for complete

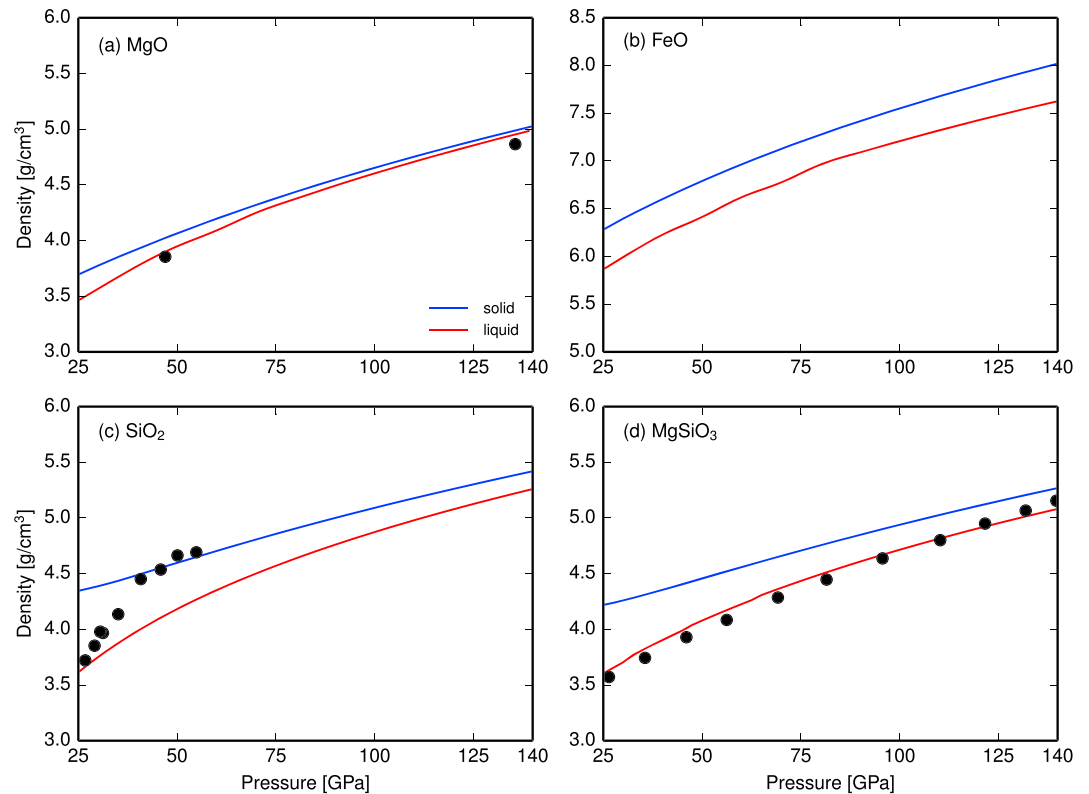


Figure 6. Predicted density profiles of (a) MgO, (b) FeO, (c) SiO₂, and (d) MgSiO₃ at melting temperature of each pressure for both solid phase (blue) and liquid phase (red). The predictions are calculated using the parameters obtained from the data set without chondritic primitive mantle, with $n = 0.5$ as an exponent of heat capacity. Densities estimated in other studies observed are also shown (filled circle, Alfè, 2005, for MgO; Sato & Funamori, 2010, for SiO₂; and Mosenfelder et al., 2009, for MgSiO₃).

solidification at 50 and 100 GPa, respectively (Figure 5d). The temperature difference between liquidus and solidus observed in chondritic PM data, on the other hand, is less than 500 K, so we suspect that their liquidus temperatures are underestimated.

The measurement of solidus temperatures is generally harder than that of liquidus (e.g., Andrault et al., 2011), indicating that the uncertainty of solidus measurements may be higher than reported. We thus conducted an additional inversion with a data set excluding solidus measurements. The smallest value of normalized cost function we achieved, however, is larger than 3. Thus, the reported liquidus temperatures for peridotite and chondritic PM, whose SiO₂ contents vary only by 7 wt%, are difficult to reconcile when they differ by more than 500 K. As discussed in section 3, the existence of other oxides is unlikely to affect the melting temperature to such a large extent.

5.2. Density Profile

Density profiles calculated using the obtained parameters demonstrate that all liquids are lighter than the corresponding solids for MgO, FeO, SiO₂, and MgSiO₃ (Figure 6). Densities estimated by the molecular dynamics simulations of Alfè (2005) and the equation of state of Mosenfelder et al. (2009) show a good agreement with our results, which are constructed just based on melting experiments. When compared with the density of amorphous SiO₂ (Sato & Funamori, 2008), however, our results show low densities over the entire pressure range. Because we aim to predict the melting for the pressure range of the entire mantle, our results may not be accurate when a transition in liquid structure occurs. Experiments suggest that amorphous SiO₂ undergoes a structural transition at around 40 GPa (Sato & Funamori, 2008), indicating that two sets of equation of state are necessary to separately describe density at low and high pressures. A much higher bulk modulus ($K = 390$ GPa at 50 GPa) suggested by their study can be explained by this as well. More data points are necessary to constrain additional parameters, and we thus plan to incorporate density

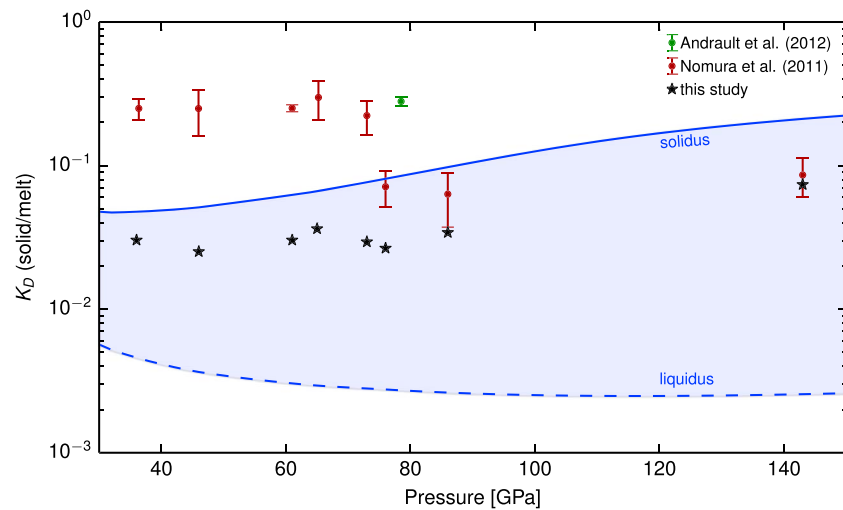


Figure 7. Partitioning of Fe and Mg between bridgmanite and melt (K_D) is calculated at the solidus (solid) and liquidus (dashed) temperatures for $(\text{Mg}_{0.88}\text{Fe}_{0.12})_2\text{SiO}_4$ olivine. The blue shaded area indicates the range of predicted values for K_D according to our thermodynamic model. Experimental results on chondritic mantle (Andrault et al., 2012, green) and olivine (Nomura et al., 2011, red) are shown as well. Because K_D takes a wide range of value in our model, partition coefficients corresponding to the conditions of Nomura et al. (2011) are also calculated (stars). The compositions of melt in equilibrium with their reported bridgmanite compositions are calculated at the same pressure and temperature conditions, from which the values of K_D are obtained.

measurements into our data set in our future study and see whether those can be reconciled with measurements on melting temperatures.

5.3. Partition Coefficients

Partitioning of Fe and Mg between melt and bridgmanite is predicted to vary by 1–2 orders of magnitude between the solidus and liquidus temperatures (Figure 7), and the partition coefficient ($K_D = (x_{\text{Fe}}^{\text{br}}/x_{\text{Mg}}^{\text{br}})/(x_{\text{Fe}}^{\text{l}}/x_{\text{Mg}}^{\text{l}})$) can be as low as 10^{-2} at the liquidus. This is because the phase loop of the MgO-FeO binary system shows a distorted shape, indicating that solid coexisting with melt is likely to be highly depleted in iron (Figure 4b). The nonidealities of MgO-SiO₂ and FeO-SiO₂ systems are not too different, so the shape of phase loop of the Mg-Fe bridgmanite binary system is expected to be similar with that of the MgO-FeO system. Experimental studies, on the other hand, suggest a drastic change in the partition coefficient for both pyrolite and olivine at pressure between 60 and 70 GPa (Nomura et al., 2011; Tateno et al., 2014), which is possibly explained by iron spin crossover in the melt phase. Because we assume the same set of thermodynamic parameters for the entire pressure range, such a discontinuity is not observed in our model, and as a result, our model may be biased to low values of K_D .

Whereas the presence of oxides with low concentrations is unlikely to affect melting temperature (section 3), its influence on element partitioning remains uncertain. An experimental study with a chondritic mantle composition suggests that the presence of aluminum can enhance the incorporation of iron in bridgmanite (Andrault et al., 2012), although other studies see no difference in partition coefficients between samples with and without aluminum (e.g., Nomura et al., 2011; Tateno et al., 2014). It has been proposed that the discrepancy may originate in how chemical analysis is conducted (Tateno et al., 2014). We also note that, in the experiments on Nomura et al. (2011), the Mg#s of both bridgmanite and melt are higher than the Mg# of the system composition, which indicates that compositional uncertainties are larger than reported. It will be necessary to expand our inverse approach to include data on partitioning experiments, so that we can quantitatively investigate the consistency of different experimental studies by taking into account the uncertainties of experimental measurements.

5.4. Outlook

With 14 thermodynamic parameters, our model successfully reproduces the given experimental data except for those of chondritic PM, though some properties of liquid are not precisely determined. For example, the formulation for heat capacity remains unconstrained because both $n = 1$ and $n = 0.5$ in equation (6) currently fit the data set equally well. The smallest misfit achieved by $n = 0.5$ ($\chi^2/N_{\text{data}} \sim 0.88$) is comparable

to the case with $n = 1$ (~ 0.81). To further constrain heat capacity, melting data on the midmantle region will be necessary; the predicted melting temperature of SiO_2 differs by up to 500 K in the midmantle region between the two cases (Figure 4d). Some molecular dynamics simulations present melting curves consistent with the case of $n = 1$ (Usui & Tsuchiya, 2010) whereas others close to the case of $n = 0.5$ (Lyzenga et al., 1983; Luo et al., 2002). If results from molecular dynamics simulations are included in our inversion, its outcome will depend on the choice of simulation studies.

There is also a possibility that the mixing behavior between MgO and FeO is not accurately described. The parameter A_{MgO} close to 1 suggests that entropy change upon melting decreases rapidly with pressure. The predicted value of ΔS at 135 GPa is $2.2 \text{ J}\cdot\text{K}^{-1}\cdot\text{mol}^{-1}$, whereas 14.9 and 25.1 are proposed by Yoshimoto (2010) and Alfè (2005), respectively. A similar trend is observed for MgSiO_3 , although other studies report very little change of ΔS with increasing pressure (Stixrude et al., 2009). The low value of our model agrees with the analysis of Deng and Lee (2017), and the discrepancy with previous studies can be attributed to experiments included in our data set. On the other hand, a negative A_{FeO} indicates that entropy change upon melting increases with pressure, which may be unlikely considering that this can be related to a larger volume change upon melting through the Clausius-Clapeyron relation. Deng and Lee (2017) argued that the usage of a regular solution model can alleviate this problem, but both models equally fit experiments well (Deng & Lee, 2017), and thus, these two models cannot be distinguished with our current approach using temperature misfit as the only criterion. Also, with the current number of data points, using additional parameters would result in larger uncertainty.

We employed 14 parameters to describe the MgO-FeO-SiO_2 ternary system in this study, yet more parameters are likely to be necessary to accurately describe the complex nature of equation of state (e.g., the nonideal mixing between MgO and FeO and possible phase transformations for SiO_2 and FeO liquids). With Al and Ca, the degree of freedom in a model will be greater, which requires our inverse approach to include more experimental constraints. Our data set is currently limited to those on solidus and liquidus temperatures, but measurements on density (e.g., Luo et al., 2004; Mosenfelder et al., 2007) and on partition coefficients (e.g., Ito et al., 2004; Liebske et al., 2005; Andraut et al., 2012) can be considered by extending our inversion strategy. Also, water is likely to play a crucial role in mantle melting (Andraut et al., 2014; Nomura et al., 2014; Pradhan et al., 2015), and the effect of water needs to be quantified in future studies.

6. Conclusion

We have presented a method to obtain a set of internally consistent thermodynamic parameters directly using experimentally determined melting temperatures. We combine the steepest descent method and Monte Carlo sampling to constrain the acceptable ranges of parameters. Our approach can handle multiple experiments with different compositions, and this enables us to make the full use of all experiments that are currently available. This also avoids being biased to a particular set of experiments, which is imperative for a better understanding of the melting of mantle materials. Our inversion scheme can also investigate the consistency of multiple experiments with different materials, and if a disagreement exists, it can be related to a certain set of thermodynamic parameters.

The uncertainty associated with each model parameter can be used to explore possible discrepancy among experiments. When our method is applied to two separate data sets, the obtained parameters are consistent with each other within uncertainty except for the thermal expansivity of SiO_2 (α_0) and the excess volume of mixing between MgO and SiO_2 ($v_0^{\text{Mg-Si}}$). On the other hand, with our parameterization of chemical potential, the parameters related to FeO are only loosely constrained and do not account for the difference in melting temperatures. We therefore predict that other oxides only have a minor effect on melting, and determining α_0 and $v_0^{\text{Mg-Si}}$ is particularly important for constraining mantle melting at high pressures.

References

- Abe, Y. (1997). Thermal and chemical evolution of the terrestrial magma ocean. *Physics of the Earth and Planetary Interiors*, 100, 27–39. [https://doi.org/10.1016/S0031-9201\(96\)03229-3](https://doi.org/10.1016/S0031-9201(96)03229-3)
- Alfè, D. (2005). Melting curve of MgO from first-principles simulations. *Physical Review Letters*, 94, 235701. <https://doi.org/10.1103/PhysRevLett.94.235701>

Acknowledgments

This work was sponsored by the National Science Foundation under grant EAR-1753916. This work was also supported in part by the facilities and staff of the Yale University Faculty of Arts and Sciences High Performance Computing Center. The authors thank Charles-Edouard Boukaré and an anonymous reviewer for constructive comments and suggestions, which helped improve the clarity of the manuscript. All data analyzed in this study are available in Zerr and Boehler (1993), Shen and Lazor (1995), Alfè (2005), Fischer and Campbell (2010), Usui and Tsuchiya (2010), Andraut et al. (2011), Kimura et al. (2017), and Deng and Lee (2017). Thermodynamic data for solid components are taken from Stixrude and Lithgow-Bertelloni (2011).

- Anderson, O. L. (1995). Equations of state of solids for geophysics and ceramic science. In H. Charnock, J. F. Dewey, S. Conway Morris, A. Navrotsky, E. R. Oxburgh, R. A. Price, & B. J. Skinner (Eds.), *Oxford Monograph on Geology and Geophysics* (Vol. 31). Oxford, UK: Oxford University Press.
- Andraut, D., Bolfan-Casanova, N., Lo Nigro, G., Bouhifd, M. A., Garbarino, G., & Mezouar, M. (2011). Solidus and liquidus profiles of chondritic mantle: Implication for melting of the Earth across its history. *Earth and Planetary Science Letters*, *304*, 251–259. <https://doi.org/10.1016/j.epsl.2011.02.006>
- Andraut, D., Pesce, G., Bouhifd, M. A., Bolfan-Casanova, N., Henot, J.-M., & Mezouar, M. (2014). Melting of subducted basalt at the core-mantle boundary. *Science*, *344*, 892–895. <https://doi.org/10.1126/science.1250466>
- Andraut, D., Petitgirard, S., Lo Nigro, G., Devidal, J. L., Veronesi, G., Garbarino, G., & Mezouar, M. (2012). Solid-liquid iron partitioning in Earth's deep mantle. *Nature*, *487*, 354–357. <https://doi.org/10.1038/nature11294>
- Berman, R. G., & Brown, T. H. (1984). A thermodynamic model for multicomponent melts, with application to the system CaO-Al₂O₃-SiO₂. *Geochimica et Cosmochimica Acta*, *49*, 661–678. [https://doi.org/10.1016/0016-7037\(85\)90053-5](https://doi.org/10.1016/0016-7037(85)90053-5)
- Boukaré, C.-E., Ricard, Y., & Fiquet, G. (2015). Thermodynamics of the MgO-FeO-SiO₂ system up to 140 GPa: Application to the crystallization of Earth's magma ocean. *Journal of Geophysical Research: Solid Earth*, *120*, 6085–6101. <https://doi.org/10.1002/2015JB011929>
- Canup, R. M., & Asphaug, E. (2001). Origin of the Moon in a giant impact near the end of the Earth's formation. *Nature*, *412*, 708–712.
- Cohen, R. E., & Gong, Z. (1994). Melting and melt structure of MgO at high pressures. *Physical Review B*, *50*, 12,301–12,311. <https://doi.org/10.1103/PhysRevB.50.12301>
- de Koker, N., Karki, B. B., & Stixrude, L. (2013). Thermodynamics of the MgO-SiO₂ liquid system in Earth's lowermost mantle from first principles. *Earth and Planetary Science Letters*, *361*, 58–63. <https://doi.org/10.1016/j.epsl.2012.11.026>
- de Koker, N., & Stixrude, L. (2009). Self-consistent thermodynamic description of silicate liquids, with application to shock melting of MgO periclase and MgSiO₃ perovskite. *Geophysical Journal International*, *178*, 162–179. <https://doi.org/10.1111/j.1365-246X.2009.04142.x>
- Deng, J., & Lee, K. K. M. (2017). Viscosity jump in the lower mantle inferred from melting curves of ferropericlase. *Nature Communications*, *8*, 1997. <https://doi.org/10.1038/s41467-017-02263-z>
- Dingwell, D. B., Knoche, R., & Webb, S. L. (1993). A volume temperature relationship for liquid GeO₂ and some geophysically relevant derived parameters for network liquids. *Physics and Chemistry of Minerals*, *19*, 445–453. <https://doi.org/10.1007/BF00203184>
- Elkins-Tanton, L. T. (2012). Magma oceans in the inner solar system. *Annual Review of Earth and Planetary Sciences*, *40*, 113–139. <https://doi.org/10.1146/annurev-earth-042711-105503>
- Fiquet, G., Auzende, A. L., Siebert, J., Corgne, A., Bureau, H., Ozawa, H., & Garbarino, G. (2010). Melting of peridotite to 140 gigapascals. *Science*, *329*, 1516–1518. <https://doi.org/10.1126/science.1192448>
- Fischer, R. A., & Campbell, A. J. (2010). High-pressure melting of wüstite. *American Mineralogist*, *95*, 1473–1477. <https://doi.org/10.2138/am.2010.3463>
- Fu, S., Yang, J., Zhang, Y., Liu, J., Greenberg, E., Prakapenka, V. B., et al. (2018). Melting behavior of the lower-mantle ferropericlase across the spin crossover: Implication for the ultra-low velocity zones at the lowermost mantle. *Earth and Planetary Science Letters*, *503*, 1–9. <https://doi.org/10.1016/j.epsl.2018.09.014>
- Ghiorso, M. S., Carmichael, I. S., Rivers, M. L., & Sack, R. O. (1983). The Gibbs free energy of mixing of natural silicate liquids; an expanded regular solution approximation for the calculation of magmatic intensive variables. *Contributions to Mineralogy and Petrology*, *84*, 107–145. <https://doi.org/10.1007/BF00371280>
- Ghiorso, M. S., Hirschmann, M. M., Reiners, P. W., & Kress, V. C. (2002). The pMELTS: A revision of MELTS for improved calculation of phase relations and major element partitioning related to partial melting of the mantle to 3 GPa. *Geochemistry, Geophysics, Geosystems*, *3*(5), 1030. <https://doi.org/10.1029/2001GC000217>
- Halliday, A. N., Wänke, H., Birck, J. L., & Clayton, R. N. (2001). The accretion, composition and early differentiation of Mars. *Space Science Reviews*, *96*, 197–230. <https://doi.org/10.1023/A:1011997206080>
- Helfrich, G., & Wood, B. (1989). Subregular model for multicomponent solutions. *American Mineralogist*, *74*, 1016–1022.
- Holland, T. J. B., & Powell, R. (1998). An internally consistent thermodynamic data set for phases of petrological interest. *Journal of Metamorphic Geology*, *16*, 309–343.
- Hudon, P., Jung, I. H., & Baker, D. R. (2002). Melting of β -quartz up to 2.0 GPa and thermodynamic optimization of the silica liquidus up to 6.0 GPa. *Physics of the Earth and Planetary Interiors*, *130*, 159–174. [https://doi.org/10.1016/S0031-9201\(02\)00005-5](https://doi.org/10.1016/S0031-9201(02)00005-5)
- Ito, E., Kubo, A., Katsura, T., & Walter, M. J. (2004). Melting experiments of mantle materials under lower mantle conditions with implications for magma ocean differentiation. *Physics of the Earth and Planetary Interiors*, *143*, 397–406. <https://doi.org/10.1016/j.pepi.2003.09.016>
- Kimura, T., Ohfuji, H., Nishi, M., & Irifune, T. (2017). Melting temperatures of MgO under high pressure by micro-texture analysis. *Nature Communications*, *8*, 15735. <https://doi.org/10.1038/ncomms15735>
- Labrosse, S., Hernlund, J. W., & Coltice, N. (2007). A crystallizing dense magma ocean at the base of the Earth's mantle. *Nature*, *450*, 866–869. <https://doi.org/10.1038/nature06355>
- Liebske, C., & Frost, D. J. (2012). Melting phase relations in the MgO-MgSiO₃ system between 16 and 26 GPa: Implications for melting in Earth's deep interior. *Earth and Planetary Science Letters*, *345–348*, 159–170. <https://doi.org/10.1016/j.epsl.2012.06.038>
- Liebske, C., Schmickler, B., Terasaki, H., Poe, B. T., Suzuki, A., Funakoshi, K.-i., et al. (2005). Viscosity of peridotite liquid up to 13 GPa: Implications for magma ocean viscosities. *Earth and Planetary Science Letters*, *240*, 589–604. <https://doi.org/10.1016/j.epsl.2005.10.004>
- Luo, S.-N., Akins, J. A., Ahrens, T. J., & Asimow, P. D. (2004). Shock-compressed MgSiO₃ glass, enstatite, olivine, and quartz: Optical emission, temperatures, and melting. *Journal of Geophysical Research*, *109*, B05205. <https://doi.org/10.1029/2003JB002860>
- Luo, S.-N., Çağın, T., Strachan, A., Goddard, W. A., & Ahrens, T. J. (2002). Molecular dynamics modeling of stishovite. *Earth and Planetary Science Letters*, *202*, 147–157. [https://doi.org/10.1016/S0012-821X\(02\)00749-5](https://doi.org/10.1016/S0012-821X(02)00749-5)
- Lyzenga, G. A., Ahrens, T. J., & Mitchell, A. C. (1983). Shock temperatures of SiO₂ and their geophysical implications. *Journal of Geophysical Research*, *88*, 2431–2444. <https://doi.org/10.1029/JB088iB03p02431>
- Matsui, T., & Abe, Y. (1986). Evolution of an impact-induced atmosphere and magma ocean on the accreting Earth. *Nature*, *319*, 303–305.
- Matsumoto, M., & Nishimura, T. (1998). Mersenne twister: A 623-dimensionally equidistributed uniform pseudo-random number generator. *ACM Transactions on Modeling and Computer Simulation*, *8*, 3–30. <https://doi.org/10.1145/272991.272995>
- Miyazaki, Y., & Korenaga, J. (2017). Effects of chemistry on vertical dust motion in early protoplanetary disks. *The Astrophysical Journal*, *849*, 41. <https://doi.org/10.3847/1538-4357/aa8cd1>
- Miyazaki, Y., & Korenaga, J. (2019). On the timescale of magma ocean solidification and its chemical consequences: 2. Compositional differentiation under crystal accumulation and matrix compaction. *Journal of Geophysical Research: Solid Earth*, *124*, 3399–3419. <https://doi.org/10.1029/2018JB016928>

- Mosenfelder, J. L., Asimow, P. D., & Ahrens, T. J. (2007). Thermodynamic properties of Mg_2SiO_4 liquid at ultra-high pressures from shock measurements to 200 GPa on forsterite and wadsleyite. *Journal of Geophysical Research*, *112*, B06208. <https://doi.org/10.1029/2006JB004364>
- Mosenfelder, J. L., Asimow, P. D., Frost, D. J., Rubie, D. C., & Ahrens, T. J. (2009). The MgSiO_3 system at high pressure: Thermodynamic properties of perovskite, postperovskite, and melt from global inversion of shock and static compression data. *Journal of Geophysical Research*, *114*, B01203. <https://doi.org/10.1029/2008JB005900>
- Murnaghan, F. D. (1951). *Finite deformation of an elastic solid* (pp. 1–140). New York: John Wiley.
- Nakajima, M., & Stevenson, D. J. (2015). Melting and mixing states of the Earth's mantle after the Moon-forming impact. *Earth and Planetary Science Letters*, *427*, 286–295. <https://doi.org/10.1016/j.epsl.2015.06.023>
- Nomura, R., Hirose, K., Uesugi, K., Ohishi, Y., Tsuchiyama, A., Miyake, A., & Ueno, Y. (2014). Low core-mantle boundary temperature inferred from the solidus of pyrolite. *Science*, *343*, 522–525.
- Nomura, R., Ozawa, H., Tateno, S., Hirose, K., Hernlund, J., Muto, S., et al. (2011). Spin crossover and iron-rich silicate melt in the Earth's deep mantle. *Nature*, *473*, 199–202. <https://doi.org/10.1038/nature09940>
- Pradhan, G. K., Fiquet, G., Siebert, J., Auzende, A. L., Morard, G., Antonangeli, D., & Garbarino, G. (2015). Melting of MORB at core-mantle boundary. *Earth and Planetary Science Letters*, *431*, 247–255. <https://doi.org/10.1016/j.epsl.2015.09.034>
- Rosenfeld, Y., & Tarazona, P. (1998). Density functional theory and the asymptotic high density expansion of the free energy of classical solids and fluids. *Molecular Physics*, *95*, 141–150. <https://doi.org/10.1080/00268979809483145>
- Rubie, D. C., Nimmo, F., & Melosh, H. J. (2015). Formation of the Earth's core. In D. C. Rubie, F. Nimmo, & H. J. Melosh (Eds.), *Treatise on geophysics, second edition* (Vol. 9, pp. 43–79). Amsterdam: Elsevier. <https://doi.org/10.1016/B978-044452748-6.00140-1>
- Sato, T., & Funamori, N. (2008). Sixfold-coordinated amorphous polymorph of SiO_2 under high pressure. *Physical Review Letters*, *101*, 255–502. <https://doi.org/10.1103/PhysRevLett.101.255502>
- Sato, T., & Funamori, N. (2010). High-pressure structural transformation of SiO_2 glass up to 100 GPa. *Physical Review B*, *82*, 184102. <https://doi.org/10.1103/PhysRevB.82.184102>
- Shen, G., & Lazor, P. (1995). Measurement of melting temperatures of some minerals under lower mantle pressures. *Journal of Geophysical Research*, *100*(B9), 17,699–17,713. <https://doi.org/10.1029/95JB01864>
- Solomatov, V. S., & Stevenson, D. J. (1993). Nonfractional crystallization of a terrestrial magma ocean. *Journal of Geophysical Research*, *98*, 5391–5406.
- Stevenson, D. J. (1987). Origin of the Moon—The collision hypothesis. *Annual Review of Earth and Planetary Sciences*, *15*, 271–315.
- Stixrude, L., de Koker, N., Sun, N., Mookherjee, M., & Karki, B. B. (2009). Thermodynamics of silicate liquids in the deep Earth. *Earth and Planetary Science Letters*, *278*, 226–232. <https://doi.org/10.1016/j.epsl.2008.12.006>
- Stixrude, L., & Lithgow-Bertelloni, C. (2011). Thermodynamics of mantle minerals—II. Phase equilibria. *Geophysical Journal International*, *184*, 1180–1213. <https://doi.org/10.1111/j.1365-246X.2010.04890.x>
- Tateno, S., Hirose, K., & Ohishi, Y. (2014). Melting experiments on peridotite to lowermost mantle conditions. *Journal of Geophysical Research: Solid Earth*, *119*, 4684–4694. <https://doi.org/10.1002/2013JB010616>. Received
- Tonks, W. B., & Melosh, H. J. (1993). Magma ocean formation due to giant impacts. *Journal of Geophysical Research*, *98*, 5319–5333. <https://doi.org/10.1029/92JE02726>
- Tronnes, R. G., & Frost, D. J. (2002). Peridotite melting and mineral-melt partitioning of major and minor elements at 22–24.5 GPa. *Earth and Planetary Science Letters*, *197*, 117–131. [https://doi.org/10.1016/S0012-821X\(02\)00466-1](https://doi.org/10.1016/S0012-821X(02)00466-1)
- Usui, Y., & Tsuchiya, T. (2010). Ab initio two-phase molecular dynamics on the melting curve of SiO_2 . *Journal of Earth Science*, *21*, 801–810. <https://doi.org/10.1007/s12583-010-0126-9>
- Wade, J., & Wood, B. J. (2005). Core formation and the oxidation state of the Earth. *Earth and Planetary Science Letters*, *236*, 78–95. <https://doi.org/10.1016/j.epsl.2005.05.017>
- Warren, P. H. (1985). The magma ocean concept and lunar evolution. *Annual Review of Earth and Planetary Science*, *13*, 201–40. <https://doi.org/10.1146/annurev.earth.13.1.201>
- Yoshimoto, Y. (2010). Melting of MgO studied using a multicanonical ensemble method combined with a first-principles calculation. *Journal of the Physical Society of Japan*, *79*, 34602.
- Zerr, A., & Boehler, R. (1993). Melting of (Mg, Fe) SiO_3 -perovskite to 625 kilobars: Indication of a high melting temperature in the lower mantle. *Science*, *262*, 553–555.
- Zerr, A., Diegeler, A., & Boehler, R. (1998). Solidus of Earth's deep mantle. *Science*, *281*, 243–246. <https://doi.org/10.1126/science.281.5374.243>